A&A 472, 797–803 (2007)
DOI: 10.1051/0004-6361:20077394

Astronomy & Astrophysics

AGN counts at 15 μm

XMM observations of the ELAIS-S1-5 sample[⋆]

F. La Franca[1], S. Puccetti[2,⋆⋆], N. Sacchi[1], C. Feruglio[3], F. Fiore[3], C. Gruppioni[4],
A. Lamastra[1], I. Matute[5], G. Melini[1], and F. Pozzi[4,6]

[1] Dipartimento di Fisica, Università Roma Tre, via della Vasca Navale 84, 00146 Roma, Italy
e-mail: `lafranca@fis.uniroma3.it`
[2] ASI Science Data Center, via Galileo Galilei, 00044, Frascati, Italy
[3] INAF – Osservatorio Astronomico di Roma, via Frascati 33, 00040 Monteporzio Catone, Italy
[4] INAF, Osservatorio Astronomico di Bologna, via Ranzani 1, 40127 Bologna, Italy
[5] INAF, Osservatorio Astrofisico di Arcetri, Largo E. Fermi 5, 50125 Firenze, Italy
[6] Dipartimento di Astronomia, Università di Bologna, via Ranzani 1, 40127 Bologna, Italy

Received 2 March 2007 / Accepted 2 June 2007

ABSTRACT

Context. The counts of galaxies and AGN in the mid infra-red (MIR) bands are important instruments for studying their cosmological evolution. However, the classic spectral line ratios techniques can become misleading when trying to properly separate AGN from starbursts or even from apparently normal galaxies.

Aims. We use X-ray band observations to discriminate AGN activity in previously classified MIR-selected starburst galaxies and to derive updated AGN1 and (Compton thin) AGN2 counts at 15 μm.

Methods. XMM observations of the ELAIS-S1 15 μm sample down to flux limits $\sim 2\times10^{-15}$ erg cm^{-2} s^{-1} (2–10 keV band) were used. We classified as AGN all those MIR sources with a unabsorbed 2–10 keV X-ray luminosity higher that $\sim 10^{42}$ erg s^{-1}.

Results. We find that at least about 13 ± 6% of the previously classified starburst galaxies harbor an AGN. According to these figures, we provide an updated estimate of the counts of AGN1 and (Compton thin) AGN2 at 15 μm. It turns out that at least 24% of the extragalactic sources brighter than 0.6 my at 15 μm are AGN (~13% contribution to the extragalactic background produced at fluxes brighter than 0.6 mJy).

Key words. cosmology: observations – infrared: galaxies – galaxies: active – surveys – galaxies: evolution – X-rays: galaxies

1. Introduction

To measure the evolution of the density of active galactic nuclei (AGN) and galaxies at various wavelengths is one of the major goals in astrophysics, and extragalactic counts in the mid-infrared (MIR) are important instruments for this. MIR surveys, carried out with the ISOCAM instrument on board the *Infrared Space Observatory* (*ISO*), indicates that the MIR galaxies have evolved significantly faster than deduced from optical surveys (e.g. Elbaz et al. 1999; Gruppioni et al. 2002; Metcalfe et al. 2003; Rodighiero et al. 2004; Pozzi et al. 2004). These results are now confirmed and extended by the data coming from the *Spitzer Space Telescope* (e.g. Gruppioni et al. 2005; Le Floc'h et al. 2005; Pérez-González et al. 2005; Babbedge et al. 2006; Caputi et al. 2007). On the contrary, the evolution of AGN at MIR wavelengths are similar to what has been measured in the optical and X-ray bands for type 1 AGN (AGN1) and even slower for type 2 AGN (Matute et al. 2002, 2006).

Proper analysis of the evolution of the sources emitting in the MIR is based on a reliable classification that allows a separation of AGN (more precisely type 2 AGN; AGN2) from the starburst galaxies. Unfortunately there is growing evidence that the classification of AGN based on their optical spectra alone provides an incomplete and sometimes deceiving description of their true nature. Indeed, some starbursts, or even normal, galaxies show signatures of a hidden AGN at non-optical wavelengths (see e.g. Moorwood et al. 1996; Marconi et al. 2000; Severgnini et al. 2003), while a fraction of X-ray selected AGN show no signatures of AGN activity in their optical spectra: the X-ray bright optically normal galaxies (XBONG, see e.g. Fiore et al. 2000; Comastri et al. 2002; La Franca et al. 2005 and references therein). Combining *Chandra* and archival X-ray data, Maiolino et al. (2003) have found that the local total density of AGN may be a factor ~2 higher than estimated from optical spectroscopic surveys. Up to now the exact proportion of AGN-dominated MIR galaxies is actually not known. This separation is also complicated by the existence of mixed systems, where both star formation and AGN activity significantly contribute to the mid-IR emission (e.g. Fritz et al. 2006; Pozzi et al. 2007).

Mid-IR studies based on *IRAS* and *ISO* observations have indirectly estimated a contribution of AGN to the cosmic infrared background (CIRB) that is not larger than 5–10% (e.g. Franceschini et al. 2001; Xu et al. 2001, 2003). This is the maximum room left in their models by the strongly evolving starburst population. The total contribution was, in any case, uncertain since mid-IR selected AGN2 and starburst galaxies were treated as a single population. A better estimate of the AGN contribution comes from the X-ray band (0.5–10 keV), which

---

[⋆] Tables 1 and 2 are only available in electronic form at
`http://www.aanda.org`

[⋆⋆] INAF personell resident at ASDC.

Article published by EDP Sciences and available at http://www.aanda.org or http://dx.doi.org/10.1051/0004-6361:20077394

offers a better wavelength regime for selecting and identifying obscured sources (unless the sources are Compton-thick, $N_{\rm H} > 10^{24}$–10^{25} cm^{-2}). A cross correlation of X-ray and IR *ISO* sources detected in deep *Chandra* and XMM-Newton observations allowed Fadda et al. (2002) to estimate that the maximum fraction of the CIRB produced by AGN is 17 ± 6%. This result is confirmed by Silva et al. (2004), who used the X-ray AGN luminosity function (LF) and semi-empirical SEDs (linking the X-ray to the Infrared) to derive that the contribution of AGN and their *host* galaxy to the CIRB is 10–20% in the 1–20 μm range. These results recently have been confirmed and extended by the analysis of joint *Spitzer* and X-ray data, where a contribution of 3–11% is derived (see e.g. Treister et al. 2006; Barmby et al. 2006; Brand et al. 2006).

On the other hand, it has been proposed that heavily X-ray obscured sources could be selected in the mid-infrared band where the dust heated by the AGN produces a spectral energy distribution (SED) that peaks at shorter wavelengths than the SED produced by dust heated by starbursts. Recently *Spitzer* data have been used to find highly obscured AGNs, both trough mid-infrared color selection (e.g. Stern et al. 2005; Polletta et al. 2006; Alonso-Herrero et al. 2006; Lacy et al. 2007) and joint radio-infrared selection (e.g. Donley et al. 2005; Weedman et al. 2006; Martinez-Sansigre et al. 2005, 2006). However, recent studies are showing that the situation is not simple. The selection of AGN with mid-IR colors is showing up as not simultaneously complete and reliable; and, moreover, when X-ray data are available, the AGN mid-IR SED do not directly correspond to the X-ray spectral type (absorbed/un-absorbed; e.g. Barmby et al. 2006; Donley et al. 2007).

In this framework it is interesting to work out more reliable AGN1 and AGN2 counts in the MIR using the 2–10 keV X-ray luminosity as a solid indication of nuclear activity. In this work we use XMM-Newton observations of the S1 area of the *European Large Area ISO Survey* (ELAIS hereafter; Oliver et al. 2000; Rowan-Robinson et al. 2004) to revise the optical spectroscopic classification of the 15 μm sample presented by La Franca et al. (2004) and then to derive new, more reliable extragalactic counts of AGN1 and not heavily absorbed ($\log N_{\rm H} < 24$ cm^{-2}, not Compton thick) AGN2 in the 0.5–10 mJy regime, where no other "class-separated" data exist at the moment.

The MIR and X-ray data are presented in Sect. 2. In Sect. 3, we describe the X-ray properties of the MIR sources, while the revised AGN 15 μm counts are derived in Sect. 4. Section 5 contains our comments and conclusions. Unless otherwise stated, all quoted errors are at the 68% confidence level. We assume $H_0 = 70$ km s^{-1} Mpc^{-1}, $\Omega_{\rm m} = 0.3$, and $\Omega_\Lambda = 0.7$.

2. The data

2.1. The 15 μm sample

The mid-IR selected sources used in this work have been extracted from the 15 μm sample selected in the central region 5 of the field S1 of the ELAIS. The 15 μm catalogue in the ELAIS S1 field has been released by Lari et al. (2001). It covers an area of ~4 deg^2 centered at $\alpha(2000) = 00^{\rm h}34^{\rm m}44.4^{\rm s}$, $\delta(2000) = -43°28'12''$ and includes 462 mid-IR sources down to a flux limit of 0.5 mJy. Mid-IR source counts based on this catalogue have been presented and discussed by Gruppioni et al. (2002). La Franca et al. (2004) presents the optical and spectroscopic identifications and classification of a more reliable subsample of 406 sources from the Lari et al. (2001) catalogue. About 80% of these sources have been optically identified on CCD exposures down to $R \sim 23$. The spectral classification has been obtained for 90% of the optically identified sample. As discussed by La Franca et al. (2004), due to a different mid-IR flux limit coverage of the ELAIS-S1 field, the total area has been divided into two regions: the central and deepest region of S1 (S1-5) reaching mid-IR fluxes (S_{15} hereafter) of 0.5 mJy, and the outer region (S1-rest) with a 0.9 mJy flux limit. The S1-5 area is spectroscopically complete at the 97% level down to $R = 21.6$, while S1-rest completeness reaches the 98% level down to $R = 20.5$. In total, 116 sources (29% of the total mid-IR sample) do not have a spectroscopic identification due to incompleteness of the follow-up or to the lack of optical counterpart brighter than $R = 23$. A detailed description of the optical identification, spectroscopic classification, size, and completeness function of the different areas used in the ELAIS-S1 sample are presented and discussed by La Franca et al. (2004).

Classification for AGN-dominated sources in the ELAIS fields was based on their optical spectral signatures. Sources showing broad emission line profiles (rest frame $FWHM >$ 1200 km s^{-1}) were classified as type-1. Type-2 sources were selected following classic diagnostic diagrams (e.g. Tresse et al. 1996; Osterbrock 1989; Veilleux & Osterbrock 1987) that included one or more of the following line ratios: [NII]/Hα, SII/(Hα+[NII]), OI/Hα, [OIII]/Hβ, and [OII]/Hβ when available, depending on the redshift of the source (e.g. $\log$([OIII]/Hβ) > 0.5 and $\log$([NII]/Hα) > –0.4).

Few objects have been re-observed in the framework of the follow-up campaign of the *Spitzer* Wide-Area Infrared Extragalactic Survey (SWIRE; see e.g. Lonsdale et al. 2003), which includes the ELAIS-S1 field. The ELAIS-S1 field has been observed in the B and V bands down to 25 Vega mag and in the R band down to 24.5 mag (Berta et al. 2006). A spectroscopic follow-up campaign was carried out in the period 2004–2006 at the 3.6 m and VLT ESO telescopes (La Franca et al. in prep.). In comparison with La Franca et al. (2004), two more 15 μm sources were spectroscopically identified in the ELAIS-S1-5 field: C15_J003317-431706 is a $R = 24.3$ galaxy showing [OII] emission at redshift 0.689, while C15_J003447-432447 is an AGN2 at redshift 1.076. Moreover, three sources with previously poor quality spectra changed their spectroscopic classification: C15_J003330-431553, which was wrongly classified as a starburst galaxy at $z = 0.473$, showed broad CIII and MgII emission at $z = 2.170$ typical of AGN1 activity; C15_J003603-433155, which was classified as AGN2, showed a broad MgII emission typical of AGN1 activity; and C15_J003622-432826, which was classified as a starburst galaxy, showed a clear [OIII]/Hβ ratio typical of AGN2 activity. In summary, the MIR sample used in this work contains 72 bona fide extragalactic sources, of which 67 sources have been optically identified down to $R \sim 25$. Fifty-seven of them have been spectroscopically identified: six are AGN1, three AGN2, while almost all of the remaining 48 sources show the emission line spectra typical of starburst activity. Most of the remaining 15 sources without spectroscopic identification (and for five sources even optical identification) are so faint that it is very likely that they are starburst galaxies at redshift higher than 0.5 (see La Franca et al. 2004).

2.2. The X-ray observations

The region S1-5 of the ELAIS was observed with the XMM-Newton telescope. The observations and data reduction are described by Puccetti et al. (2006). The region was observed by four partially overlapping pointings, covering a total area of ~0.6 deg^2 (see Fig. 1). The observations were carried out from

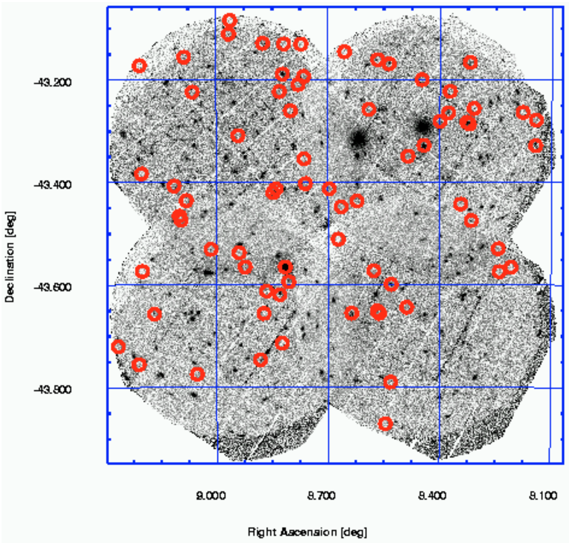

Fig. 1. Mosaic of the four XMM-Newton pointings in the ELAIS-S1 field obtained by adding up the images of the PN and MOS cameras in the energy range 0.5–10 keV (Puccetti et al. 2006). The circles are the position of the 72 15 μm ELAIS extragalactic sources.

May to July 2003, and each pointing lasted 84–100 ks. Source detection was performed on Co-added PN+MOS1+MOS2 images accumulated in four energy bands: 0.5–10 keV, 0.5–2 keV, 2–10 keV, and 5–10 keV. In total 478 sources were detected with a significance level[1] of 2×10^{-5}. The flux limits are 5.5×10^{-16} erg cm^{-2} s^{-1} in the 0.5–2 keV band, 2×10^{-15} erg cm^{-2} s^{-1} in the 2–10 keV band, and 4×10^{-15} erg cm^{-2} s^{-1} in the 5–10 keV band.

The source counts in each camera were obtained using the events files in the energy range 0.5–10 keV for the PN and 0.3–10 keV for the MOS. The counts of the two MOS cameras were eventually combined. The counts of each source were extracted in a circular region with a radius in the range 20″–30″. In general, the radius value was chosen so that the S/N ratio was roughly optimized, but this choice was limited in a few cases by the presence of nearby sources or by a peculiar position of the source on the detector, for example close to a gap in the CCD array. In some cases the source was detected, and the corresponding counts extracted, only in either the PN or in one or both of the MOS cameras, because PN and MOS do not cover exactly the same sky regions and the position of the gaps differs in the PN, MOS1, and MOS2 CCD arrays.

The background counts for each source were extracted from the nearest source-free region. In doing so, areas near gaps in the CCD array and near the edge of the telescope field of view have been excluded, as well as regions containing hot pixels and other CCD cosmetic defects.

The ancillary response files were generated for each source by means of the tool ARFGEN, in order to properly correct for energy-dependent vignetting and point spread function. The response matrix files were generated with the tool RMFGEN (SAS 6.1.0[2]).

The spectral counts, when higher than about 120, were first accumulated in energy bins with 20 counts each, from 0.3 keV to 10 keV in the MOS and from 0.5 to 10 keV in the PN. They were then fitted, using XSPEC (version 11.3.1) and the χ^2 statistic with a model comprising, in addition to the known galactic absorption ($\sim 2.76 \times 10^{20}$ cm^{-2}): (1) a power law, with two parameters, normalization and photon spectral index Γ; (2) the absorption $N_{\rm H}$ at the redshift of the source. Sometimes a thin plasma model with the temperature as a parameter was added. In the case of degrees of freedom lower than 12, a fixed photon index $\Gamma = 1.8$ was assumed. When both PN and MOS data were available, their relative normalization MOS/PN was left free to vary between 0.8 and 1.2. This interval was conservatively chosen wider than applicable on-axis, because a fully reliable intercalibration is still lacking for sources off-axis. When the spectral counts were lower than about 120, the C statistic (Cash 1979) was used instead, as implemented in XSPEC (Arnaud 2003[3]) after background subtraction (see Alexander et al. 2003a, for a similar procedure) and with 5 counts in each energy bin (the latter choice was made only for convenience; it does not impair the correct use of the embedded statistics when using the above-mentioned XSPEC implementation).

3. X-ray properties of the 15 μm sources

We wish to use the X-ray observations to identify possible AGN activity among those 15 μm galaxies whose optical spectroscopic identification did no show any AGN signatures. We have thus chosen a lower limit intrinsic un-absorbed X-ray luminosity of $\sim 10^{42}$ erg s^{-1} in order to classify a source as an AGN. Indeed higher luminosities are typical of AGN activity (see e.g. Ranalli et al. 2003; Maiolino et al. 2003), while the most X-ray-luminous star-forming galaxy known, NGC 3256, has a total X-ray luminosity of $L_{\rm X} \simeq 8 \times 10^{41}$ erg s^{-1} (Lira et al. 2002).

In total, 13 out of the 72 XMM observed ELAIS 15 μm sources were detected in the X-ray band. Table 1 shows the X-ray and optical spectral characteristics for each X-ray detected source. For the remaining 59 X-ray undetected ISO sources, three sigma-confidence level upper limits have been measured in the 0.5–10 keV and 2–10 keV energy bands. Table 2 shows a summary for all 72 ELAIS sources of the MIR, optical and X-ray fluxes and luminosities. The redshift and optical spectroscopic classification is given when available. The X-ray luminosities of the detected sources have been corrected for absorption.

Twelve of the 13 X-ray detected sources have an optical and spectroscopic identification, while the X-ray detected source C15_J003315-432829 has an optical counterpart with $R = 21.61$ but no optical spectroscopic identification. Figure 2 shows the redshift of the spectroscopically identified ELAIS sources as a function of the optical or MIR fluxes. As it is possible to see, all sources with R-band magnitude fainter than $R = 20.5$ have redshift higher than 0.45. Then, as discussed by La Franca et al. (2004), this (not classified) source (C15_J003315-432829) is likely to be a starburst galaxy or an AGN2 at redshift higher than 0.5. According to this guess, a lower limit of $10^{43.4}$ erg s^{-1} on the X-ray luminosity is derived. This result allowed us to classify this source as an AGN. Anyhow, for the sake of our analyses, even an assumed redshift as low as 0.2 would imply an X-ray luminosity higher than 10^{42} erg s^{-1}, typical of AGN activity, and does not change our conclusions.

Four out of the six previously optically-classified AGN1 were detected in the X-ray band and have 2–10 keV luminosities higher than $10^{43.2}$ erg s^{-1}. Their X-ray spectral shape confirms

---

[1] This corresponds to about one spurious source over each of the four XMM-Newton fields.

[2] `http://xmm.vilspa.esa.es/external/xmm_sw_cal/sas_frame.shtml`

[3] K.A. Arnaud, 2003, "XSPEC User Guide for version 11.3" `http://heasarc.gsfc.nasa.gov/docs/software/lheasoft/xanadu/~xspec/manual/manual.html`

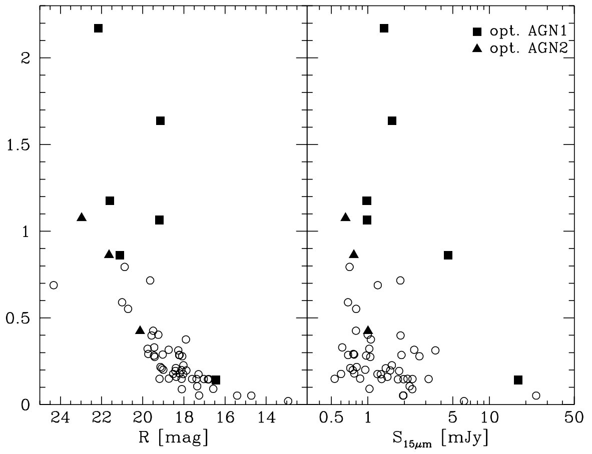

Fig. 2. *Left*. Redshift versus *R*-band magnitude distribution of the 15 μm sources. Filled squares and triangles are optically classified AGN1 and AGN2, respectively. Open circles are optically classified starburst galaxies. *Right*. Redshift versus 15 μm flux distribution of the 15 μm sources. Symbols are as in the previous panel.

this classification, although two AGN1, C15_J003330-431553 and C15_J003640-433925, show absorbed spectra with column densities of $\log N_{\rm H} \sim 23$ cm^{-2}. This result is not so unusual for AGN1 (see La Franca et al. 2005, and references therein). The remaining two undetected AGN1 and the three (previously optically classified) AGN2 have 2–10 keV X-ray-luminosity upper limits of $\sim 10^{43.2}$–$10^{44.0}$ erg s^{-1}, which are still consistent with the typical X-ray luminosity of un-absorbed AGNs (10^{42}–10^{46} erg s^{-1}).

All the 9 remaining X-ray detected sources have the optical spectra typical of starburst activity. However, eight of them have X-ray luminosities typical of AGN activity: five showed absorbed ($\log N_{\rm H} \geq 22$ cm^{-2}) X-ray spectra, thus reinforcing the classification as AGN2, while the other three sources have X-ray spectra consistent with an unabsorbed power law. Finally, the last source (C15_J003432-433922) has the X-ray luminosity typical of starburst activity ($\sim 10^{40}$ erg s^{-1}). This is also confirmed by its X-ray spectrum, where a thin plasma model (MEKAL with $KT = 0.60^{+1.11}_{-0.35}$) has necessarily been added to the power-law model.

There are 14 sources without X-ray detections and without measured redshift. According to either their *R*-band optical magnitudes or their *R*-band magnitude limits ($R > 24.5$), most of these sources should lie at redshifts higher than 0.5 (see discussion in La Franca et al. 2004). In order to derive an upper limit on their X-ray luminosities, we made the conservative assumption that these sources lie at redshift 1.2. According to this assumption, the corresponding 2–10 keV unabsorbed X-ray luminosity upper limits are always greater than 10^{43} erg s^{-1} (see Fig. 3), and then no conclusion on their nature can be derived from the X-ray observations.

Figure 3 shows the 2–10 keV unabsorbed luminosity as a function of the redshift and MIR luminosities. For 59 sources, we have only upper limits on the X-ray fluxes and, then, on the *un-absorbed* X-ray luminosities (using the measured redshifts or, when not available, a conservative estimate of $z = 1.2$). However these estimates do not take the effects of possible X-ray absorption into account . This effect is more relevant at low redshifts ($z < 0.5$–1) because the absorption mainly affects the rest-frame, lower-energy photons that are instead no longer observable in the 2–10 keV band at higher redshift.

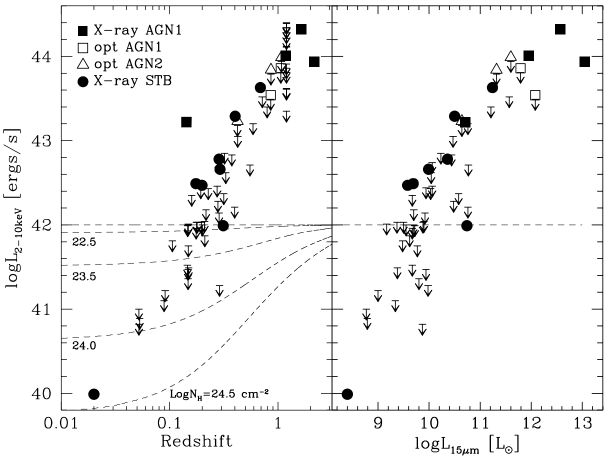

Fig. 3. *Left*. 2–10 keV X-ray luminosity versus redshift. Squares are AGN1, triangles are optically classified AGN2, and circles are galaxies. Filled symbols are X-ray detected sources. The dashed lines show our AGN luminosity threshold, and the expected observed X-ray luminosity as a function of absorption and redshift of an absorbed source having an intrinsic X-ray luminosity of 10^{42} erg s^{-1}. *Right*. 2–10 keV X-ray luminosity versus 15 μm luminosity of the ELAIS-S1-5 sources. Symbols are as in the previous panel.

In Fig. 3 (left) the expected observed X-ray luminosity is shown as a function of absorption and the redshift of an absorbed source having an intrinsic X-ray luminosity of 10^{42} erg s^{-1}. We can expect 50% less emission at redshift $z \sim 0.5$ for a Compton-thin source with a column density of $\mathrm{Log}\, N_{\rm H} = 23.5$ cm^{-2}. In this case a $\sim 10^{41.7}$ erg s^{-1} absorbed luminosity would be observed. The only solution for detecting such low redshift-absorbed AGN would be to obtain deeper X-ray observations in order to analyze their X-ray spectra and separate X-ray luminous star-forming galaxies from absorbed AGN. As expected, the situation is even worst for Compton-thick ($\mathrm{Log}\, N_{\rm H} > 24$ cm^{-2}), absorbed AGN: in this case the fluxes would be reduced by more than a factor of ten. We thus conclude that our X-ray observations are only able to detect a relevant, but nevertheless incomplete, fraction of the Compton-thin AGN. Then our attempt to identify the population of AGN missed by the optical spectroscopic identifications is partly inefficient, limited to un-absorbed, or Compton-thin, absorbed AGN. Therefore, the densities of AGN derived in the next sections are only to be considered lower limits.

4. Discussion

4.1. The newly classified AGN

We observed 72 ELAIS sources with XMM-Newton. Nine sources, previously classified in the optical as AGN (6 AGN1 and 3 AGN2) showed X-ray properties (either detections or upper limits) in agreement with their optical classification. Eight out of the 63 previously classified (or bona fide) starburst galaxies instead showed X-ray luminosities typical of AGN activity. As our optical spectroscopic studies were sensitive enough to detect broad emission lines (see La Franca et al. 2004), we classified them as new AGN2. As discussed in the previous section, the object C15_J003315-432829 has no spectroscopic identification, but its X-ray flux is so bright that will have an X-ray luminosity higher than 10^{42} erg s^{-1} at redshifts higher than $z = 0.2$. We inspected the optical spectra of the remaining seven new AGN2 (see Fig. 4). C15_J003317-431706 was observed after the publication of the spectroscopic catalogue by

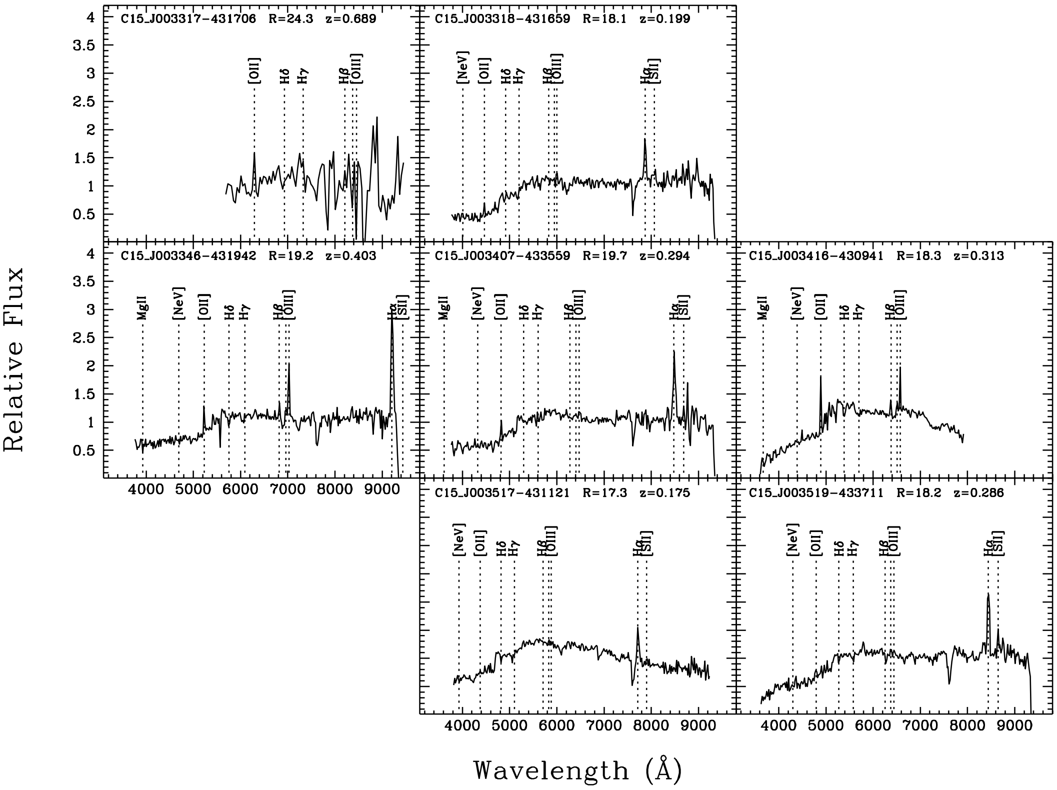

Fig. 4. Optical spectra of the seven objects showing AGN X-ray luminosity and previously classified as no-AGN galaxies. The position of the typical emission lines of AGN (even if not observed) are shown.

La Franca et al. (2004) and is an $R = 24.3$ galaxy at $z = 0.689$ observed by VIMOS at VLT (see Sect. 2.1). It has a noisy spectrum, just showing a clear [OII]λ3727 emission line, which hampers a more detailed classification. According to the classification scheme used by La Franca et al. (2004; see also Dressler et al. 1999; Poggianti et al. 1999), the remaining six galaxies are: two e(a) dust-enshrouded starburst galaxies, three e(c) star-forming spirals, and one k(e) post-starburst galaxy with emission lines. C15_J003346-431942, which was classified as an e(a) galaxy, has the line ratios typical of a LINER, but could be compatible with an AGN2 classification if 10% errors are taken into account. C15_J003318-431659, which was classified as an e(c) galaxy (showing no detectable Hβ emission or absorption) has a limit on the [OIII]5007/Hβ ratio which is compatible with an AGN2. On the contrary, even taking the line ratio uncertainties into account, the remaining five objects do not show any signature in the optical spectrum compatible with an AGN activity.

As shown in Fig. 5, according to the large statistical uncertainties, there is no significant dependence on the 15 μm flux by the fraction of the newly X-ray classified AGN2. We can then conclude that at least a constant fraction of $12.7^{+6.3}_{-4.4}$% of the previously optically-classified starburst galaxies are instead AGN2.

According to our X-ray luminosities' upper limits or measurements, all galaxies with $L_{15} < 10^{9.5}\ L_{\odot}$ are unlikely to harbor an AGN (see Fig. 3). In contrast, all the newly classified AGN2 have IR luminosities in the range $10^{9.5}\ L_{\odot} < L_{15} < 10^{11}\ L_{\odot}$, exactly in the region of the AGN2 LF where a flattening has been observed (Matute et al. 2006). This result confirms the hypothesis of Matute et al. (2006) that the observed flattening of the AGN2 LF at redshift ~0.35 was due to an incompleteness in the AGN identification. As previously pointed out by La Franca et al. (2004), the origin of this incompleteness has to be ascribed to the fact that a relevant fraction of AGN2 do not show clear AGN signatures in their optical spectra.

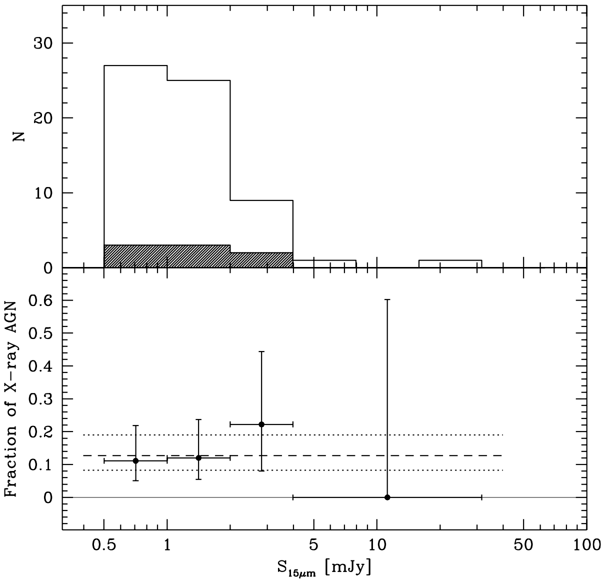

Fig. 5. *Up*. Flux distribution of the 63 ELAIS-S1-5 sources that were not optically classified as AGN. The shaded histogram shows the flux distribution of the eight sources that showed AGN activity in the X-ray band. *Down*. Fraction of the X-ray active AGN among the galaxies as a function of the 15 μm flux. The long dashed line shows the adopted average constant value of 12.7%, while the dotted lines are 1σ confidence-level uncertainties.

The more IR luminous objects in our sample are AGN1, which show 15 μm luminosities higher than $10^{11.5}\ L_{\odot}$.

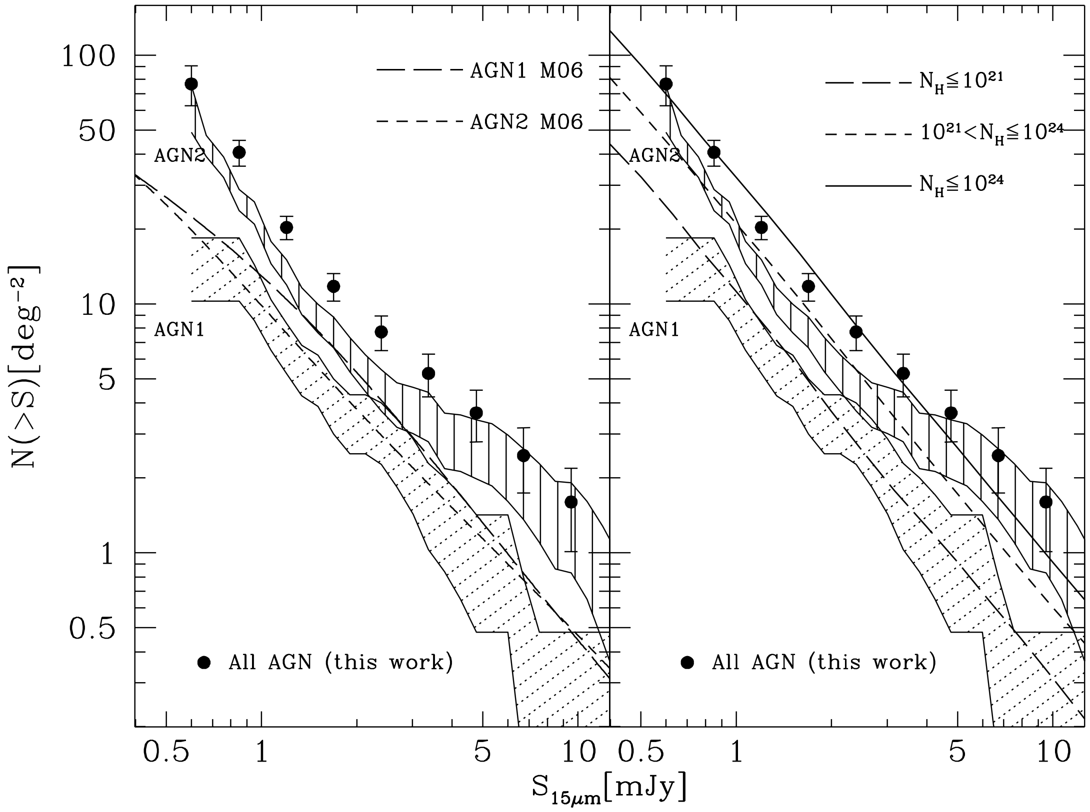

Fig. 6. Revised AGN1 and (Compton thin) AGN2 integral counts at 15 μm. Filled circles are the total (AGN1+AGN2) counts. *Left.* The short and long dashed lines are the predicted AGN1 and AGN2 counts, respectively, by Matute et al. (2006). *Right.* The short and long dashed lines are the predicted un-absorbed and Compton thin counts, respectively, by Silva et al. (2004) on the basis of the X-ray AGN luminosity function and semi-empirical SEDs (linking the X-ray to the infrared). The continuous line is the prediction of the total AGN counts (including Compton-thin absorbed sources) by Silva et al. (2004).

As discussed by Matute et al. (2006), the absence of AGN2 in this luminosity range is mainly due to selection effects. The AGN1 SEDs have a fairly constant infrared to optical ratio, while for AGN2 the infrared-to-optical ratio increases with the increase in the luminosity ($\mathrm{Log}\,(L_{15}/L_R) \propto 0.5\ \mathrm{Log}\,L_{15}$). As a consequence, AGN2 have on average fainter optical counterparts than AGN1 at high luminosities and then miss the spectroscopic identification (see Fig. 1 in Matute et al. 2006).

4.2. Revised AGN 15 μm counts

According to this above new classification, we have then corrected the integral 15 μm counts, previously derived from the optical spectroscopic classification of the ELAIS-S1 sources by La Franca et al. (2004). According to the estimates described in the previous section, we have assumed that 12.7% of all ELAIS-S1 optically classified or bona fide starburst galaxies harbor an AGN2. The results are presented in Table 3 and shown in Fig. 6. The newly derived counts are compared in Fig. 6 (left) with the predictions from the AGN1 and AGN2 luminosity functions computed by Matute et al. (2006), and in Fig. 6 (right) with the AGN counts predicted by Silva et al. (2004) on the basis of the X-ray AGN luminosity function (LF) and semi-empirical SEDs (linking the X-ray to the infrared). It turns out that the AGN1 counts agree, within the uncertainties, with the counts predicted by both the AGN1 LF of Matute et al. (2006) and the un-absorbed ($N_{\rm H} \leq 10^{21}$ cm^{-2}) AGN of Silva et al. (2004). Conversely, the new AGN2 counts are, as expected, about a factor of 2–3 higher than predicted by the AGN2 LF of Matute et al. (2006). At fluxes larger than 0.6 mJy, the density of AGN2 is about 60 deg^{-2}, while Matute et al. (2006) predict a density of about 20 deg^{-2}. On the other hand, the predicted count of absorbed, Compton-thin AGN ($10^{21} < N_{\rm H} < 10^{24}$ cm^{-2}) by Silva et al. (2004) are consistent with our estimates of the AGN2 counts.

Table 3. AGN1 and AGN2 integral counts at 15 μm.

S_{15} mJy	AGN1 $N(>S)$ deg^{-2}	AGN2 $N(>S)$ deg^{-2}
0.60	14.4 ± 4.1	62 ± 13
0.76	14.4 ± 4.1	35.6 ± 3.4
0.95	11.5 ± 2.9	23.3 ± 2.4
1.20	6.8 ± 1.6	13.5 ± 1.6
1.51	5.1 ± 1.3	8.8 ± 1.2
1.90	3.41 ± 0.91	6.3 ± 1.0
2.39	3.14 ± 0.87	4.58 ± 0.86
3.01	2.15 ± 0.72	3.82 ± 0.81
3.79	1.42 ± 0.58	2.91 ± 0.73
4.77	0.95 ± 0.47	2.70 ± 0.72
6.00	0.95 ± 0.47	2.29 ± 0.68
7.55	0.24 ± 0.24	1.69 ± 0.59
9.51	0.24 ± 0.24	1.37 ± 0.54

All the extragalactic sources, with 15 μm fluxes brighter than 0.6 mJy, produce a 15 μm background of $\nu I(\nu) = 0.343\mathrm{nW\,m^{-2}\,sm^{-1}}$, while the AGNs produce $\nu I(\nu) = 0.046\mathrm{nW\,m^{-2}\,sm^{-1}}$ (~13% contribution to the extragalactic background produced at fluxes brighter than 0.6 mJy).

5. Conclusions

We have used XMM-Newton observations of the 15 μm sample of the ELAIS-S1-5 area to disentangle AGN activity among previously spectroscopically classified starburst galaxies. We find that at least a fraction of 13 ± 6% (not dependent on the flux) of the previously spectroscopically classified starburst galaxies are instead bona fide (Compton thin) AGN2. The fraction of newly identified AGN2 is not large enough to significantly change the results previously found by Pozzi et al. (2004) for the evolution of the LF of the starburst galaxies obtained by using the ELAIS sample. On the other hand, as the density of galaxies is about an order of magnitude higher than the density of AGN at 15 μm fluxes of ~1 mJy, the new density of AGN2 is significantly increased by a factor of ~2–3. This result agrees with the analysis of Matute et al. (2006), who ascribe the observed flattening of the AGN2 LF at redshifts ~0.5 to an incompleteness of the optical spectroscopic identification techniques.

Here we wish to focus on the two results: a) that more than half of the AGN2 could miss their classification if only the optical spectra were used and b) that, according to our analysis and predictions derived from the hard X-ray luminosity function, the surface density of (Compton thin) AGN2 at fluxes larger than 0.6 mJy is in the range 50–70 deg^{-2}. These are the first estimates of separated AGN1 and AGN2 counts in the MIR. This result corresponds to a fraction of about 24% (17/72) of AGN (AGN1 plus AGN2) among all the extragalactic sources at 15 μm fluxes larger than 0.6 mJy (~13% contribution to the extragalactic background produced at fluxes brighter than 0.6 mJy).

According to our analysis, the ongoing studies of the density and evolution of absorbed/reddened AGN (AGN2) among the *Spitzer* sources, if only based on optical spectroscopic identifications, would miss about half of the true AGN2. A more efficient approach would require MIR color-selection criteria, or better if complemented with deep hard X-ray observations (see e.g. Barmby et al. 2006; Donley et al. 2007; Fiore et al. 2007; Daddi et al. 2007).

Acknowledgements. We thank Laura Silva for discussions and for having provided the predictions of the 15 μm AGN counts in machine-readable format. We thank the anonymous referee for the useful comments. This research has been partially supported by ASI, INAF, and MIUR grants.

References

Alonso-Herrero, A., Pérez-González, P. G., Alexander, D. M., et al. 2006, ApJ, 640, 167
Babbedge, T. S. R., Rowan-Robinson, M., Vaccari, M., et al. 2006, MNRAS, 370, 1159
Barmby, P., Alonso-Herrero, A., Donley, J. L., et al. 2006, ApJ, 642, 126
Berta, S., Rubele, S., Franceschini, A., et al. 2006, A&A, 451, 881
Brand, K., Dey, A., Weedman, D., La Franca, F., Vignali, C., et al. 2006, ApJ, 644, 143
Caputi, K. I., Lagache, G., Yan, Lin, et al. 2007, ApJ, 660, 97
Comastri, A., Mignoli, M., Ciliegi, P., et al. 2002, ApJ, 571, 771
Daddi, E., et al. 2007, ApJ, submitted, [`arXiv:0705.2832`]
Donley, J. L., Rieke, G. H., Rigby, J. R., & Pérez-González, P. G. 2005, ApJ, 634, 169
Donley, J. L., Rieke, G. H., Pérez-González, P. G., Rigby, J. R., & Alonso-Herrero, A., 2007, ApJ, 660, 167
Dressler, A., Smail, I., Poggianti, B. M., et al. 1999, ApJS, 122, 51
Elbaz, D., Cesarsky, C. J., Fadda, D., et al. 1999, A&A, 351, L37
Fadda, D., Flores, H., Hasinger, G., et al. 2002, A&A, 383, 838
Fiore, F., La Franca, F., Vignali, C., et al. 2000, NewA, 5, 143
Fiore, F., Brusa, M., Cocchia, F., et al. 2003, A&A, 409, 79
Fiore, F., et al. 2007, ApJ, submitted, [`arXiv:0705.2864`]
Franceschini, A., Aussel, H., Cesarsky, C. J., Elbaz, D., & Fadda, D. 2001, A&A, 378, 1
Fritz, J., Franceschini, A., & Hatziminaoglou, E. 2006, MNRAS, 366, 767
Gruppioni, C., Lari, C., Pozzi, F., et al. 2002, MNRAS, 335, 831
Gruppioni, C., Pozzi, F., Lari, C., Oliver, S., & Rodighiero, G. 2005, ApJ, 618, L9
La Franca, F., Gruppioni, C., Matute, I., et al. 2004, AJ, 127, 3705
La Franca, F., Fiore, F., Comastri, A., et al. 2005, ApJ, 635, 864
Lacy, M., Storrie-Lombardi, L. J., et al. 2004, ApJS, 154, 166
Lacy, M., Petric, A. O., Sajina, A., et al. 2007, AJ, 133, 186
Lari, C., Pozzi, F., Gruppioni, C., et al. 2001, MNRAS, 325, 1173
Le Floc'h, E., Papovich, C., Dole, H., et al. 2005, ApJ, 632, 169
Lira, P., Ward, M., Zezas, A., Alonso-Herrero, A., & Ueno, S. 2002, MNRAS, 330, 259
Lonsdale, C. J., Smith, H. E., Rowan-Robinson, M., et al. 2003, PASP, 115, 897
Maiolino, R., Comastri, A., Gilli, R., et al. 2003, MNRAS, 344, L59
Marconi, A., Oliva, E., van der Werf, P. P., et al. 2000, A&A, 357, 24
Martínez-Sansigre, A., Rawlings, S., Lacy, M., et al. 2005, Nature, 436, 666
Martínez-Sansigre, A., Rawlings, S., Lacy, M., et al. 2006, MNRAS, 370, 1479
Matute, I., La Franca, F., Pozzi, F., et al. 2002, MNRAS, 332, L11
Matute, I., La Franca, F., Pozzi, F., et al. 2006, A&A, 451, 443
Metcalfe, L., Kneib, J.-P., McBreen, B., et al. 2003, A&A, 407, 791
Moorwood, A. F. M., Lutz, D., Oliva, E., et al. 1996, A&A, 315, L109
Oliver, S., Rowan-Robinson, M., Alexander, D. M., et al. 2000, MNRAS, 316, 749
Osterbrock, D. E. 1989, Astrophysics of Gaseous Nebulae and Active Galactic Nuclei (Mill Valley: Univ. Sci.)
Pérez-González, P. G., Rieke, G. H., Egami, E., et al. 2005, ApJ, 630, 82
Poggianti, B. M., Smail, I., Dressler, A., et al. 1999, ApJ, 518, 576
Polletta, M., Wilkes, B. J., Siana, B., et al. 2006, ApJ, 642, 673
Pozzi, F., Gruppioni, C., Oliver, S., et al. 2004, ApJ, 609, 122
Pozzi, F., Vignali, C., Comastri, A., et al. 2007, A&A, 468, 603
Puccetti, S., Fiore, F., D'Elia, V., et al. 2006, A&A, 457, 501
Ranalli, P., Comastri, A., & Setti, G. 2003, A&A, 399, 39
Rodighiero, G., Lari, C., Franceschini, A., Gregnanin, A., & Fadda, D. 2003, MNRAS, 343, 1155
Rowan-Robinson, M., Lari, C., Perez-Fournon, I., et al. 2004, MNRAS, 351, 1290
Sajina, A., Lacy, M., & Scott, D. 2005, ApJ, 621, 256
Severgnini, P., Caccianiga, A., Braito, V., et al. 2003, A&A, 406, 483
Silva, L., Maiolino, R., & Granato, G. L. 2004, MNRAS, 355, 973
Stern, D., Eisenhardt, P., Gorjian, V., et al. 2005, ApJ, 631, 163
Treister, E., Urry, C. M., Van Duyne, J., et al. 2006, ApJ, 640, 603
Tresse, L., Rola, C., Hammer, F., et al. 1996, MNRAS, 281, 847
Ueda, Y., Akiyama, M., Ohta, K., & Miyaji, T. 2003, ApJ, 598, 886
Veilleux, S., & Osterbrock, D. E. 1987, ApJS, 63, 295
Weedman, D., Polletta, M., Lonsdale, C. J.; et al. 2006, ApJ, 653, 101
Xu, C. K., Lonsdale, C. J., Shupe, D. L., O'linger, J., & Masci, F. 2001, ApJ, 562, 179
Xu, C. K., Lonsdale, C. J., Shupe, D. L., Polletta, M., Lonsdale, C. J., et al. 2003, ApJ, 587, 90

Online Material

Table 1. X-ray detected sources.

Name (1)	$\alpha_{\rm MIR}$ (2)	$\delta_{\rm MIR}$ (3)	$\alpha_{\rm X}$ (4)	$\delta_{\rm X}$ (5)	Δ (6)	Γ (7)	*KT* (8)	$N_{\rm H}$ (9)	χ^2/d.o.f. (10)	$F_{0.5-10}$ (11)	F_{2-10} (12)	*z* (13)	$L_{0.5-10}$ (14)	L_{2-10} (15)	$Cl_{\rm O}$ (16)	$Cl_{\rm X}$ (17)
C15_J003234-431940	8.143084	–43.327194	8.14298	–43.32731	0.5	1.80	...	$0.00^{0.43}_{0.00}$	6.8/10	2.28	1.44	1.637	44.53	44.32	1	AGN1
C15_J003315-432829	8.315042	–43.475304	8.31612	–43.47545	2.9	$2.37^{4.22}_{2.00}$	...	$8.0^{20.2}_{7.5}$	10.6/14	1.81	1.69	>0.5	>43.78	>43.40	...	AGN
C15_J003317-431706	8.321417	–43.285069	8.31999	–43.28590	4.8	1.80	...	$4.32^{1.66}_{1.21}$	2.0/4	2.49	2.28	0.689	43.68	43.63	5	AGN2
C15_J003318-431659	8.326542	–43.284195	8.32648	–43.28473	1.9	1.80	...	$3.39^{1.25}_{0.98}$	27.3/27	2.38	2.24	0.199	42.68	42.47	5	AGN2
C15_J003330-431553	8.376667	–43.265110	8.37693	–43.26542	1.3	1.80	...	$7.2^{12.8}_{5.1}$	12.3/22	0.43	0.34	2.170	44.21	43.94	1	AGN1
C15_J003346-431942	8.442875	–43.328835	8.44301	–43.32917	1.3	$1.49^{0.16}_{0.10}$	...	$0.00^{0.10}_{0.00}$	60.9/61	5.44	3.97	0.403	43.43	43.29	3	AGN2
C15_J003407-433559	8.530666	–43.599583	8.53035	–43.59983	1.2	$2.02^{1.07}_{0.60}$	...	$1.45^{1.68}_{0.97}$	26.5/31	1.89	1.54	0.294	42.94	42.66	5	AGN2
C15_J003416-430941	8.566916	–43.161446	8.56900	–43.16218	6.1	1.80	...	$0.02^{1.03}_{0.02}$	3.0/4	0.32	0.05	0.313	42.20	42.00	3	AGN2
C15_J003432-433922	8.635791	–43.656029	8.63476	–43.65776	6.8	1.80	$0.60^{1.11}_{0.35}$	$0.00^{0.12}_{0.00}$	8.1/8	2.01	1.07	0.020	40.28	39.99	6	STB
C15_J003515-433356	8.815042	–43.566029	8.81537	–43.56558	1.8	$2.68^{0.04}_{0.00}$	...	$0.00^{0.00}_{0.00}$	285/160	86.24	27.62	0.143	43.75	43.22	1	AGN1
C15_J003517-431121	8.821792	–43.189335	8.82196	–43.18954	0.9	$1.90^{0.22}_{0.10}$	...	$0.00^{0.04}_{0.00}$	52.7/56	6.15	3.66	0.175	42.73	42.49	6	AGN2
C15_J003519-433711	8.830126	-43.619667	8.82976	–43.61887	3.0	1.80	...	$2.04^{1.11}_{0.79}$	13.7/11	2.52	2.22	0.286	42.98	42.78	5	AGN2
C15_J003640-433925	9.168375	–43.657333	9.16840	–43.65727	0.2	1.80	...	$10.8^{13.5}_{4.7}$	28.1/26	1.47	1.34	1.181	44.20	44.01	1	AGN1

Notes. The columns are as follows: (1) ELAIS ID name; (2, 3) Right Ascension and Declination at 15 μm (deg); (4, 5) Right Ascension and Declination in the 0.5–10 keV band; (6) distance of the MIR and X-ray sources (arcsec); (7) photon spectral index; (8) temperature of the MEKAL model (keV); (9) $N_{\rm H}$ column densities in 10^{22} cm^{-2} units; (10) χ^2 and degrees of freedom of the XSPEC fit; (11, 12) 0.5–10 keV and 2–10 keV band fluxes in 10^{-14} erg/s/cm^2 units; (13) redshift; (14, 15) log of the 0.5–10 keV band and 2–10 keV band luminosity in erg/s units; (16) optical spectroscopic class as in La Franca et al. (2004) (1 = AGN1, 2 = AGN2, 3 = e(a) gal, 4 = e(b) gal, 5 = e(c) gal, 6 = k(e) gal, 7 = k gal); (17) optical plus X-ray final classification.

Table 2. X-ray properties of the 15 μm sources.

Name (1)	F_{15} (2)	R (3)	z (4)	Cl (5)	L_{15} (6)	L_R (7)	$F_{0.5-10}$ (8)	F_{2-10} (9)	$L_{0.5-10}$ (10)	L_{2-10} (11)
ELAISC15_J003234-431642	1.18	19.12	...	0	...	...	<0.61	<1.62	<43.86	<44.28
ELAISC15_J003234-431940	1.58	19.15	1.637	1	12.57	12.29	2.28	1.44	44.53	44.32
ELAISC15_J003242-431548	0.71	20.88	0.794	4	11.21	11.17	<0.43	<0.96	<43.05	<43.40
ELAISC15_J003249-433201	1.65	23.70	...	0	...	...	<0.49	<1.36	<43.76	<44.21
ELAISC15_J003257-433426	0.77	18.21	0.180	5	9.50	10.22	<0.72	<1.23	<41.80	<42.03
ELAISC15_J003258-433145	0.77	19.03	0.289	5	9.98	10.41	<0.12	<0.08	<41.49	<41.28
ELAISC15_J003314-431522	1.40	19.08	0.210	6	9.90	10.03	<0.65	<0.90	<41.90	<42.04
ELAISC15_J003315-432829	2.50	21.61	>0.5	0	...	...	1.81	1.69	>43.78	>43.40
ELAISC15_J003316-430959	1.53	17.88	0.197	6	9.88	10.44	<1.03	<1.01	<42.04	<42.03
ELAISC15_J003317-431706	1.21	24.33	0.689	5	11.24	9.51	2.49	2.28	43.68	43.63
ELAISC15_J003318-431659	0.75	18.12	0.199	5	9.58	10.36	2.38	2.24	42.68	42.47
ELAISC15_J003322-432633	2.41	18.74	0.316	3	10.58	10.63	<0.39	<0.77	<42.08	<42.37
ELAISC15_J003329-431322	0.72	18.39	0.211	6	9.62	10.31	<0.11	<0.60	<41.12	<41.87
ELAISC15_J003330-431553	1.36	22.16	2.170	1	13.05	12.76	0.43	0.34	44.21	43.94
ELAISC15_J003335-431653	0.87	18.73	0.150	5	9.38	9.82	<0.50	<0.52	<41.47	<41.49
ELAISC15_J003346-431942	1.00	19.24	0.403	3	10.50	10.74	5.44	3.97	43.43	43.29
ELAISC15_J003347-431201	0.81	19.14	0.217	5	9.70	10.04	<0.58	<1.13	<41.89	<42.18
ELAISC15_J003356-432058	2.33	17.03	0.148	5	9.80	10.49	<0.33	<0.40	<41.28	<41.36
ELAISC15_J003357-433839	0.81	21.87	...	0	...	...	<0.30	<0.35	<43.55	<43.61
ELAISC15_J003401-430846	1.95	14.72	0.052	7	8.77	10.41	<0.41	<1.58	<40.42	<41.00
ELAISC15_J003407-433559	0.76	19.73	0.294	5	9.99	10.15	1.89	1.54	42.94	42.66
ELAISC15_J003407-434725	0.80	20.71	0.552	3	10.77	10.61	<0.24	<0.46	<42.43	<42.71
ELAISC15_J003408-431011	0.99	19.20	1.065	1	11.79	11.75	<0.44	<1.39	<43.36	<43.86
ELAISC15_J003410-435217	1.08	...	...	0	...	...	<0.13	<0.35	<43.19	<43.62
ELAISC15_J003414-433012	0.65	22.80	...	0	...	...	<0.35	<1.08	<43.61	<44.11
ELAISC15_J003416-430941	3.60	18.27	0.313	3	10.74	10.80	0.32	0.05	42.20	42.00
ELAISC15_J003416-433905	1.03	16.57	0.091	5	9.00	10.19	<0.80	<0.82	<41.21	<41.22
ELAISC15_J003417-433422	0.53	19.18	0.149	3	9.17	9.63	<0.40	<1.77	<41.37	<42.01
ELAISC15_J003421-431531	3.16	17.38	0.148	6	9.94	10.35	<0.48	<0.51	<41.44	<41.47
ELAISC15_J003429-432614	24.32	15.41	0.052	5	9.87	10.13	<0.75	<1.04	<40.68	<40.82
ELAISC15_J003432-433922	6.19	12.93	0.020	6	8.40	10.25	2.01	1.07	40.28	39.99
ELAISC15_J003439-432654	1.96	17.26	0.053	6	8.79	9.41	<0.56	<1.17	<40.57	<40.89
ELAISC15_J003441-433041	1.45	18.37	0.160	6	9.67	10.03	<4.57	<3.26	<42.49	<42.35
ELAISC15_J003447-432447	0.65	22.97	1.076	2	11.60	10.86	<0.98	<1.96	<43.71	<43.99
ELAISC15_J003502-432411	1.58	18.02	0.227	5	10.03	10.54	<0.90	<1.84	<42.12	<42.43
ELAISC15_J003503-432117	1.77	16.83	0.146	5	9.67	10.55	<0.14	<0.60	<40.90	<41.52
ELAISC15_J003503-431138	1.20	18.03	0.176	5	9.67	10.27	<0.61	<1.09	<41.71	<41.96
ELAISC15_J003505-430752	1.03	19.76	0.322	3	10.23	10.24	<1.67	<2.23	<42.73	<42.85
ELAISC15_J003507-431236	0.60	18.52	0.177	3	9.37	10.08	<0.73	<1.26	<41.79	<42.03
ELAISC15_J003512-431540	1.05	19.42	0.275	6	10.06	10.19	<0.61	<1.27	<42.13	<42.46
ELAISC15_J003513-433540	1.97	16.78	0.147	6	9.72	10.58	<1.70	<1.72	<41.98	<41.99
ELAISC15_J003515-433356	17.32	16.43	0.143	1	10.71	10.66	86.24	27.62	43.75	43.22
ELAISC15_J003516-430750	0.96	24.88	...	0	...	...	<0.35	<0.55	<43.61	<43.81
ELAISC15_J003517-431121	1.28	17.29	0.175	6	9.69	10.56	6.15	3.66	42.73	42.49
ELAISC15_J003517-434252	1.30	17.60	0.148	6	9.55	10.26	<1.26	<1.73	<41.86	<42.00
ELAISC15_J003519-433711	1.89	18.21	0.286	5	10.36	10.72	2.52	2.22	42.98	42.78
ELAISC15_J003519-431325	2.66	18.08	0.279	6	10.48	10.74	<0.86	<0.83	<42.30	<42.28
ELAISC15_J003520-433645	2.12	18.11	0.149	3	9.77	10.06	<0.59	<0.96	<41.54	<41.75
ELAISC15_J003521-432447	2.32	18.10	0.089	4	9.34	9.56	<0.40	<0.65	<40.89	<41.10
ELAISC15_J003523-432514	0.97	19.45	0.283	3	10.06	10.21	<1.34	<2.32	<42.51	<42.74
ELAISC15_J003529-433923	0.58	...	...	0	...	...	<0.26	<0.62	<43.49	<43.86
ELAISC15_J003529-430746	0.95	19.00	0.201	3	9.69	10.02	<0.71	<0.90	<41.90	<42.00
ELAISC15_J003531-434448	0.69	18.23	0.286	5	9.92	10.71	<0.52	<0.56	<42.10	<42.14
ELAISC15_J003541-433302	1.85	19.64	0.716	3	11.57	11.48	<1.29	<1.60	<43.42	<43.52
ELAISC15_J003545-433216	1.86	19.57	0.399	4	10.76	10.59	<0.24	<0.31	<42.10	<42.21

Table 2. continued.

Name (1)	F_{15} (2)	R (3)	z (4)	Cl (5)	L_{15} (6)	L_R (7)	$F_{0.5-10}$ (8)	F_{2-10} (9)	$L_{0.5-10}$ (10)	L_{2-10} (11)
ELAISC15_J003545-431833	0.74	21.46	...	0	...	...	<0.36	<0.19	<43.62	<43.35
ELAISC15_J003548-430640	0.80	19.49	0.426	3	10.47	10.71	<0.89	<1.84	<42.74	<43.05
ELAISC15_J003550-430505	1.00	20.13	0.425	2	10.64	10.34	<1.48	<2.84	<42.95	<43.23
ELAISC15_J003603-433152	4.59	21.11	0.860	1	12.08	10.81	<0.38	<1.09	<43.07	<43.54
ELAISC15_J003612-434627	1.18	24.27	...	0	...	...	<0.58	<1.11	<43.83	<44.12
ELAISC15_J003615-431327	0.62	19.44	0.330	5	10.04	10.40	<0.38	<1.24	<42.11	<42.62
ELAISC15_J003619-432608	2.21	17.35	0.106	3	9.48	10.03	<0.66	<2.28	<41.27	<41.81
ELAISC15_J003620-430920	0.76	...	...	0	...	...	<1.11	<1.84	<44.12	<44.34
ELAISC15_J003622-432826	0.77	21.64	0.863	2	11.32	11.02	<2.12	<2.15	<43.83	<43.84
ELAISC15_J003623-432702	0.69	21.00	0.590	3	10.76	10.60	<0.12	<1.21	<42.19	<43.20
ELAISC15_J003627-432426	0.71	22.46	...	0	...	...	<1.05	<2.14	<44.09	<44.40
ELAISC15_J003640-433925	0.98	21.59	1.181	1	11.95	10.93	1.47	1.34	44.20	44.01
ELAISC15_J003647-433424	0.74	...	...	0	...	...	<0.79	<2.10	<43.97	<44.39
ELAISC15_J003650-434519	0.92	...	...	0	...	...	<0.37	<0.69	<43.64	<43.91
ELAISC15_J003656-434312	1.06	17.90	0.376	5	10.44	11.18	<1.03	<1.48	<42.67	<42.83
ELAISC15_J003648-432259	1.57	24.35	...	0	...	...	<0.74	<1.86	<43.94	<44.34
ELAISC15_J003649-431018	1.81	18.41	0.194	4	9.94	10.22	<0.97	<2.69	<42.00	<42.44

Notes. The columns are as follows: (1) ELAIS ID name; (2) 15 μm flux in mJy units; (3) R-band magnitude; (4) redshift; (5) optical spectroscopic class as in La Franca et al. (2004) (1 = AGN1, 2 = AGN2, 3 = e(a) gal, 4 = e(b) gal, 5 = e(c) gal, 6 = k(e) gal, 7 = k gal); (6) 15 μm luminosity in solar units; (7) R-band luminosity in solar units; (8) 0.5–10 keV band flux in 10^{-14} erg/s/cm^2 units; (9) 2–10 keV band flux in 10^{-14} erg/s/cm^2 units; (10) log of the 0.5–10 keV band luminosity in erg/s units; (11) log of the 2–10 keV band luminosity in erg/s units.